ELSEVIER

Contents lists available at ScienceDirect

Surface & Coatings Technology

journal homepage: www.elsevier.com/locate/surfcoat





Printability of $Zr_{41.2}Ti_{13.8}Cu_{12.5}Ni_{10.0}Be_{22.5}$ metallic glass on steel by laser additive manufacturing: A single-track study

Shengbiao Zhang, Peijun Hou, Shahryar Mooraj, Wen Chen

Department of Mechanical and Industrial Engineering, University of Massachusetts, Amherst, MA 01003, USA

ARTICLE INFO

Keywords:
Metallic glass
Laser additive manufacturing
Single track
Printability
Numerical simulation

ABSTRACT

The amorphous structure of metallic glasses (MGs) endows them with extraordinary properties. Formation of MGs requires sufficiently high cooling rates to bypass crystallization, which results in their limited sizes by conventional processing routes such as casting. Laser additive manufacturing (LAM) technique is featured by high solidification rate that provides the potential for scalable fabrication of MGs. In this work, through high throughput laser single-track melting experiments, we studied the LAM processing window of a Zr_{41.2}Ti_{13.8}. Cu_{12.5}Ni_{10.0}Be_{22.5} (at.%) MG to achieve materials with near-full density and minimal crystallization. We observed different types of single-track features including cracking, lack-of-fusion, and partial crystallization under different combinations of laser processing parameters. To rationalize the processing-structure relationships during LAM of MGs, finite-element thermal modeling was performed to monitor the transient temperature evolution and site-specific cooling rate in the melt pool. Our work provides significant insight into the LAM protocol optimization towards fully amorphous, well-bonded, and dense MG coatings on dissimilar crystalline materials.

1. Introduction

Metallic glasses (MGs) are non-equilibrium metal alloys that are rapidly cooled from liquid melts. The disordered atomic structure of MGs endows them with a gamut of extraordinary properties such as high strength (>1 GPa), high elasticity (\sim 2%), strong corrosion resistance, and thermoplastic-like formability in the supercooled liquid state [1–5]. However, the requirement of rapid cooling for glass formation leads to limited specimen dimensions, which restricts their widespread applications [6–8].

Laser additive manufacturing (LAM) is an emerging 3D printing technology that enables fabrication of net-shaped materials with complex geometries directly from digital models [9–12]. The cooling rate during LAM is usually orders of magnitude higher than that in traditional casting, reaching 10^4 – 10^6 K/s [9] that provides great potential to process MGs at large scale. In recent years, LAM of MGs has garnered increasing interest [13–22]. Near-fully amorphous MGs with sizes that exceed the critical casting thickness has been successfully achieved by LAM [13,23]. However, partial crystallization and processing-induced defects such as micro-cracking remain acute challenges [13,16,17,24,25]. It has been widely recognized that partial

crystallization in MGs, despite some exceptions, often leads to detrimental embrittlement [26,27]. How to mitigate the processing defects and minimize crystallization are still open questions. From processing standpoint, materials are built layer-by-layer during LAM, whereby repeated melting and solidification of highly localized melt pools constitute the unit processes of single tracks. As a consequence, the solidification microstructure development of the melt pool in the singletrack deposition provides basic information that is essential for understanding the additively manufactured material property at bulk scale. In fact, single-track studies have been widely adopted for LAM of a wide range of metal alloys including steels [28,29], Ti-alloys [30,31], Alalloys [32,33], Ni-based superalloys [34,35], and MGs [36]. In general, the temperature evolution in the melt pool is site-dependent, which can give rise to highly heterogeneous microstructure. For example, in additively manufactured crystalline metals, large variations in thermal gradient and solidification velocity from the melt pool boundary to melt pool center result in the frequently observed columnar-to-equiaxed grain morphology transition [9]. Nevertheless, the processing defects and microstructure evolution, and their correlations with the sitedependent thermal history in the melt pool of MGs during LAM remain elusive. Furthermore, less crystallization and better interfacial

E-mail address: wenchen@umass.edu (W. Chen).

^{*} Corresponding author.

bonding are two key factors in achieving wear resistance of high quality. However, the former requires higher cooling rate, while the latter needs higher energy input, which will lead to lower cooling rate. Studies have been carried out for the balance. Sohrabi et al. [37] realized well-bonded Zr-based MG coatings on Al substrate with a large amorphous fraction by a two-layer coating via LAM; Li et al. [38] found higher substrate temperature gave rise to a stronger bond between MG coating and substrate during LAM.

In this work, we studied the microstructure and mechanical property (microhardness) of high-throughput laser single-tracks of $Zr_{41.2}Ti_{13.8}$. $Cu_{12.5}Ni_{10.0}Be_{22.5}$ (at.%, trade name Vitreloy1) [39] MG deposited on a dissimilar low-carbon steel substrate under a wide range of LAM processing parameters in an effort to identify the effective single-track processing window for minimal processing defects and crystallization. Vitreloy1 MG was selected due to its excellent glass forming ability and processability [39]. In addition, numerical simulation is a useful tool to monitor temperature history of melt pool [40–42], so we performed finite-element thermal modeling to examine the transient time-temperature profile and the corresponding site-specific cooling rates throughout the melt pool. The systematic study by combining high-throughput experiments and thermal simulation provides mechanistic insight into the processing-structure-property relationships in laser additively manufactured MGs on dissimilar crystalline materials.

2. Methodology

2.1. Experimental

The $Zr_{41.2}Ti_{13.8}Cu_{12.5}Ni_{10.0}Be_{22.5}$ (at.%) ingot was prepared from high-purity elements (higher than 99.9%) via arc melting, then the ingot was gas-atomized by high-purity argon to obtain amorphous powders. The oxygen content was measured by instrumental gas analysis to be approximately $\sim\!0.04$ wt%. Fig. 1a shows the morphology of the powders by scanning electron microscopy (SEM). The powders are predominantly spherical with smooth surface, indicative of good flowability. The powders with a size range of 15–53 μ m were used for our experiment. The X-ray diffraction (XRD) pattern of the as-received powders consists of a broad diffused halo peak, suggesting the fully amorphous structure at the detection limit of XRD (Fig. 1b).

Single-track experiments were conducted using an Optomec Laser Engineered Net Shaping (LENS) 450 system containing a 400 W IPG fiber laser with a wavelength of 1064 nm and a laser spot size of approximately 400 μ m at the focal point. The chamber of the Optomec LENS 450 system was filled with high-purity argon as protective gas to keep the oxygen level below 20 ppm. As well-known, MG coatings exhibit high hardness, wear resistance, and corrosion resistance [43]. To also explore the possibility to deposit MG coatings onto a crystalline substrate, we select a most-commonly used steel, low carbon steel, as a prototype steel substrate. Low carbon steel with a dimension of 4 in. \times 4

in. \times 3/16 in. (McMaster-Carr, see composition in Table 1) was used as the printing substrate. The steel substrate was polished and cleaned by acetone to remove the impurities before the single-track experiments. Vitreloy1 powders were pre-spread on the substrate with a uniform layer thickness of \sim 100 μ m. For a high-throughput study, a broad range of the LAM processing parameters were performed for single-track library depositions (see Table 2). All the single-track samples were sectioned via electrical discharge machining for compositional and microstructural analyses. The spacing between tracks was set at 4 mm to allow sufficient cooling of the tracks and marginal interactions of heat-affected zones.

The microstructure and chemical composition of the samples were characterized by an optical microscope (OM, OLYMPUS SC50) and a Magellan 400 field emission scanning electron microscope (SEM, Magellan 400 XHR-SEM) equipped with energy-dispersive X-ray spectroscopy (EDS). The cross-sections of all single-track beads were polished using SiC abrasive papers with 400, 800, and 1200 grits respectively, followed by 20 nm diamond suspension. The samples were etched with a corrosive agent (a mixture of 1 ml HNO3 and 3 ml HCl) for SEM observation. The amorphous structure of the Vitreloy1 powders was identified by X-ray diffraction (XRD, PANalytical X'Pert Pro), using a Cu-K α target with the 2θ scanning range of $20^{\circ} \sim 100^{\circ}$. In addition, the microhardness experiments across the melt pool with a spacing of 76.2 μ m (0.003 in.) were performed on a Vickers Microhardness Tester (ALPHA -MHT-2000Z) with an applied load of 0.98 N and a dwell time of 10 s.

2.2. Finite element modeling

Finite element method (FEM) based modeling was carried out to study the transient temperature development during the LAM process by ABAQUS/Standard. The geometry of the substrate was set as 7.6 mm \times 7.6 mm \times 1.6 mm in longitudinal, transverse, and normal directions, respectively. The thickness of MG powders was 0.1 mm and discretized using a 0.025 mm element size. The linear brick element with eight integration points (ABAQUS element type DC3D8) was applied in the FEM model. The temperature at the bottom of the substrate was maintained at ambient temperature (i.e., 298 K) as the boundary condition. The heat transfer in the FEM model was implemented to investigate the melt pool geometry and the cooling rate through thermal conduction, convection, and radiation applied on the top surface of the MG powders. Moreover, 15 s cooling time was applied to allow the cool-down of the temperature to ambient temperature.

The FEM simulation is based on the classic heat transfer theory, which is briefly reviewed as following. The governing equation of the heat transfer is expressed as follows:

$$\rho c_p \frac{\partial T}{\partial t} + \nabla (-k\nabla T) = q_{rad} + q_{conv} + q_{beam}$$
 (1)

where ρ is the density (5.92 g/cm³ [44]), c_p the specific heat, T the

80 90

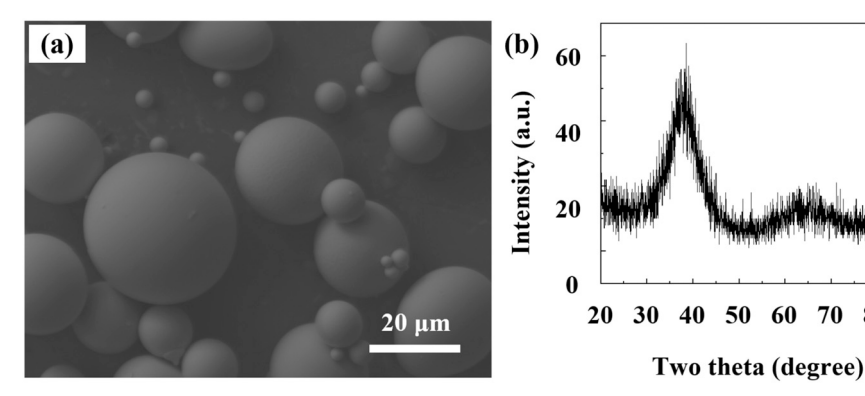


Fig. 1. (a) SEM morphology and (b) XRD pattern of the gas-atomized Vitreloy1 alloy powders.

 Table 1

 Chemical composition of the low carbon steel substrate (wt%).

Alloy	Fe	Mn	С	Cr	P	Ni	Cu	Si	S	Mo	V
Low carbon steel	99.004	0.7	0.2	0.04	0.022	0.01	0.01	0.007	0.006	0.003	0.001

 Table 2

 Processing parameters for high-throughput LAM single-track study of Vitrelov1.

Serial number	Laser power (P, W)	Scanning speed (ν , mm/ min)	Serial number	Laser power (P, W)	Scanning speed (v, mm/ min)
1	100	100	25	200	550
2	100	250	26	200	700
3	100	400	27	200	850
4	100	550	28	200	1000
5	100	700	29	225	100
6	100	850	30	225	250
7	100	1000	31	225	400
8	150	100	32	225	550
9	150	250	33	225	700
10	150	400	34	225	850
11	150	550	35	225	1000
12	150	700	36	250	250
13	150	850	37	250	400
14	150	1000	38	250	550
15	175	100	39	250	700
16	175	250	40	250	850
17	175	400	41	250	1000
18	175	550	42	300	250
19	175	700	43	300	400
20	175	850	44	300	550
21	175	1000	45	300	700
22	200	100	46	300	850
23	200	250	47	300	1000
24	200	400			

temperature, k the thermal conductivity, ∇T the gradient of the temperature field, q_{rad} and q_{conv} the convection and radiation heat flux, respectively, and q_{beam} is the Gaussian heat source.

$$q_{rad} = \epsilon \sigma_B (T^4 - T_{amb}^4) \tag{2}$$

$$q_{conv} = h(T_{amb} - T) (3)$$

and

$$q_{beam} = \alpha P \left[\frac{1}{\pi \sigma^2 d} exp\left(-\frac{x^2 + y^2}{2\sigma^2} \right) \right] exp\left(-\frac{|z|}{d} \right)$$
 (4)

where ϵ is the emissivity, $\sigma_{\rm B}$ the Stefan-Boltzmann constant, i.e.,5.67 \times 10^{-8} W/m²-K, T_{amb} the ambient temperature, h the convection heat transfer coefficient, α the laser energy absorptivity of the material affected by the wavelength of the laser, P the laser power, and σ and d the laser beam radius and depth, respectively. It should be noted that the laser beam radius σ and laser beam depth d in the Gaussian heat source used in the FEM model was calibrated through fitting the melt pool geometry from the experimental results as inputs. The thermophysical parameters such as thermal conductivity and specific heat capacity of the Vitreloy1 MG and the low-carbon steel substrate [45,46] used in the FEM simulation are all listed in Table 3.

3. Results and discussion

3.1. Printability diagram

For high-throughput LAM deposition of Vitreloy1 MG single-track library, we systematically varied the laser power from 100 W to 300 W and the scanning speed from 100 mm/min to 1000 mm/min (Fig. 2a-b). Based on the cross-sectional morphology of the melt pool, the single-

Table 3Thermophysical parameters used in the finite element modeling.

Parameter	Value		
Density (ρ , kg/m ³)	5920 (Vitreloy1) [44], 7854 (low carbon steel) [46]		
Latent heat (H, kJ/kg)	136.60 (Vitreloy1) [47], 258.9 (low carbon steel) [45]		
Solidus temperature (T_s , K)	940 (Vitreloy1) [48], 1742 (low carbon steel) [45]		
Liquidus temperature (T_l , K)	1001 (Vitreloy1) [48], 1785 (low carbon steel) [45]		
Laser power (P, W)	150		
Scanning speed (v, mm/ min)	250, 400, 1000		
Laser beam radius (σ , mm)	0.6		
Laser beam depth (d, mm)	0.7		
Emissivity (ϵ)	0.1		
Absorptivity (α)	0.75 (Vitreloy1)		

track beads are categorized into four different types: good track with marginal crystallization, good track with severe crystallization, cracking, and lack of fusion. Here, good track denotes high density sample that is free of cracking or lack-of-fusion defects. Their representative microstructures are shown in Fig. 2c-f. As presented in this printability diagram, good tracks with near-full density (>99.5%) were achieved under a laser power range of P = 150-200 W and an intermediate ratio of laser power (P) to scanning speed (ν), i.e., linear energy density of $\ensuremath{\textit{P/v}} \approx 0.2\text{--}0.6$ W·min/mm. As the laser power was increased above 200 W or P/v exceeded 0.6 W·min/mm, cracks tended to develop. These cracks originated from the melt pool boundary and some of them extended through the entire melt pool, leading to local fracture. In contrast, at lower powers of P < 150 W or $P/v < 0.2 \text{ W} \cdot \text{min/mm}$, lackof-fusion defects were observed at the interface between the substrate and melt pool. In the following, the formation of these processing defects will be discussed.

Cracking is frequently observed in additively manufactured metal alloys, especially brittle materials. The cracking behavior in the present MG single-tracks is presumably attributed to the existence of residual stresses at high laser powers and linear energy densities, as well as the brittle nature inherent to MGs. During LAM, remarkable residual stresses arise due to the differences in thermophysical properties between the Vitreloy1 MG and low carbon steel substrate, such as coefficient of thermal expansion (CTE), melting point, and thermal conductivity [17,49]. Large thermal gradients arise due to the highly localized heating and rapid cooling of a melt pool during LAM, and are subject to many processing parameters, such as laser power, melt pool size, powder thermophysical characteristics, etc. [50]. Upon rapid solidification, the thermal contraction of the melt pool is constrained by the substrate, giving rise to the compressive residual stresses on the top surface and tensile residual stresses at the bottom [51]. The magnitude of such residual stresses scales directly with the thermal gradient, which is proportional to the applied laser power and linear energy density [52]. Once the residual stresses exceed the yield stress of the melt pool, plastic yielding and cracks may be developed [25,51,53]. In crystalline metals, the thermal residual stresses during LAM can be often released by plastic deformation in the form of dislocation nucleation and multiplication [54]. In contrast, MGs are typically very brittle with a limited plastic zone size, ahead of which cracks can propagate rapidly towards the center of the melt pool [55]. Interestingly, we found that the observed cracks in the MG single-tracks appear to initiate from the melt pool boundary, whereby preferential crystallization was concurrently revealed (see Fig. 3 later). This observation is understandable since the melt pool boundary is featured by the largest thermal gradient and CTE

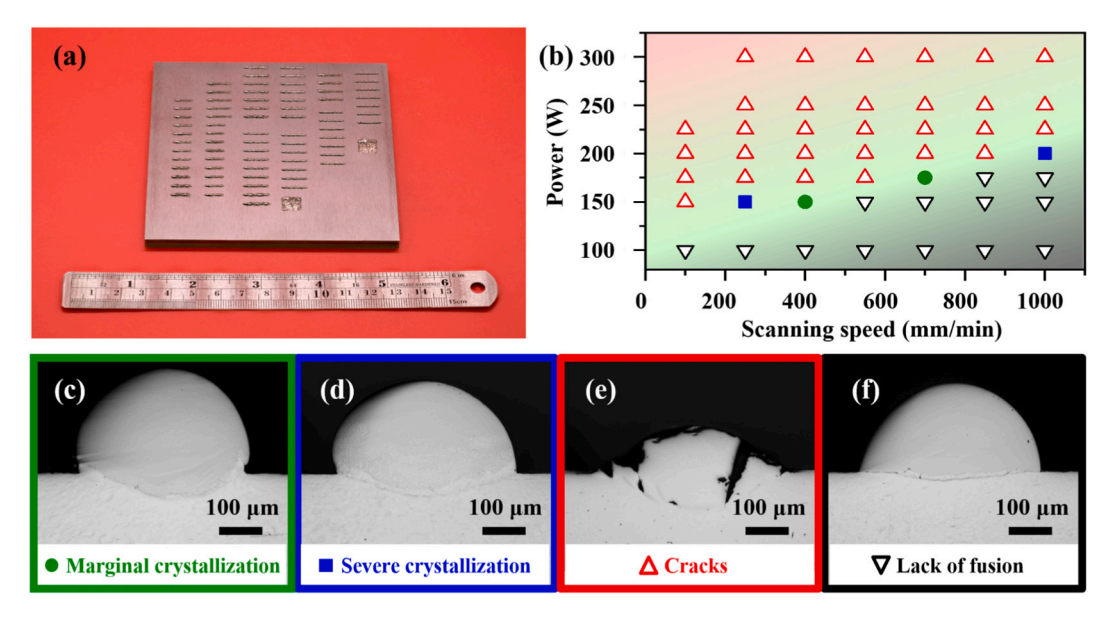


Fig. 2. (a) Library image of all single-tracks of Vitreloy1 MG. (b) Printability diagram with representative single-track morphologies: (c) good single-track with marginal crystallization (P = 150 W, $\nu = 400 \text{ mm/min}$), (d) good single-track with severe crystallization (P = 150 W, $\nu = 250 \text{ mm/min}$), (e) single-track with cracking defects (P = 225 W, $\nu = 850 \text{ mm/min}$) and (f) single-track with lack-of-fusion defects (P = 150 W, $\nu = 1000 \text{ mm/min}$).

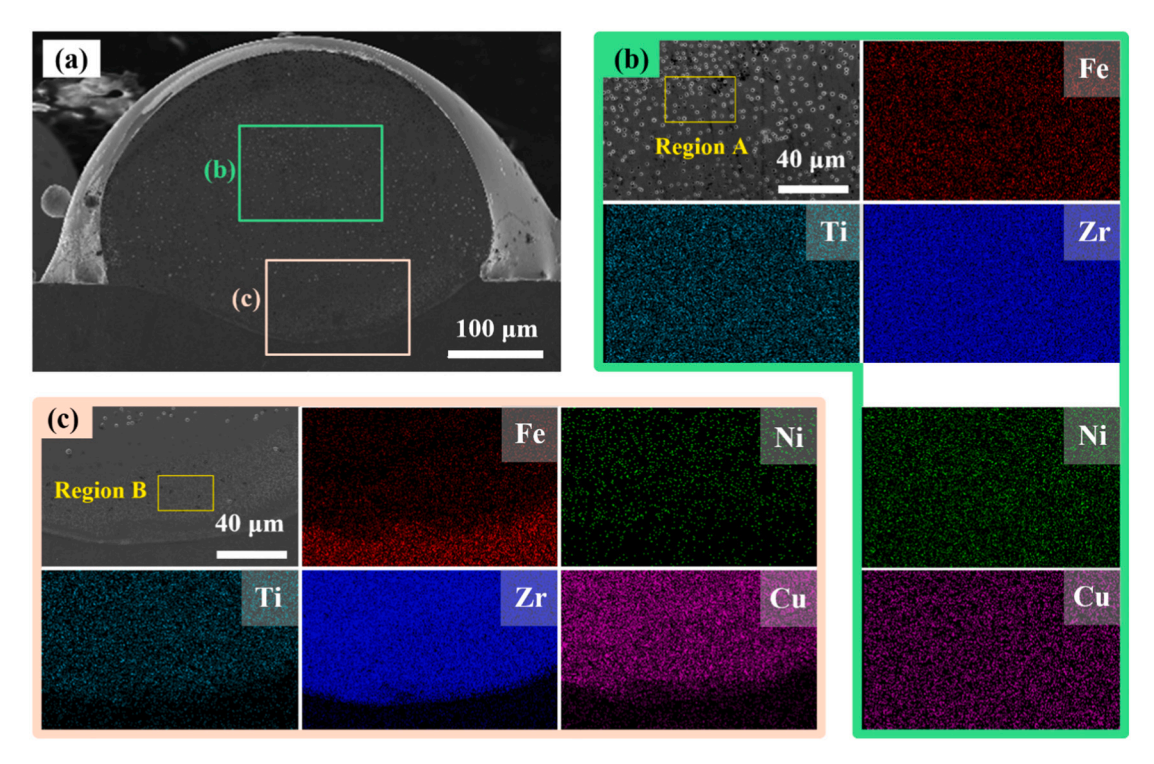


Fig. 3. (a) Cross-sectional SEM micrograph of Vitreloy1 single-track with marginal crystallization (P = 150 W, v = 400 mm/min). (b) SEM-EDS mapping of the area marked by the shallow-grape box in (a). (c) SEM-EDS mapping of the area marked by the shallow-orange box in (a). The average elemental compositions of Region A in (b) and Region B in (c) are summarized in Table 4. (For interpretation of the references to colour in this figure legend, the reader is referred to the web version of this article.)

mismatch between the MG and the steel substrate, as well as lowest solidification rate that may readily trigger crystallization [56–58]. In this context, the partially crystallized products (e.g., intermetallics) become even more brittle to accelerate the crack initiation [27,59]. The site-specific thermal schedule and cooling rate throughout the melt pool will be discussed in Section 3.3 by finite-element thermal modeling.

Lack-of-fusion defects occurred at the melt pool boundary when P < 150 W or P/v < 0.2 W·min/mm (Fig. 2b). In this case, the energy of the

incident laser beam is insufficient to melt the substrate to a significant depth to enable metallurgical bond between the single-track bead and the substrate, leading to linear-shaped voids at the interface [60]. In this study, lack-of-fusion defects were present when the melt pool dimension followed D/t < 1.5, where D and t correspond to the melt pool depth and powder layer thickness (i.e., 100 μ m), respectively. Interestingly, such observation agrees well with the melt pool geometry criterion for lack-of-fusion formation in laser additively manufactured crystalline metals

[61]. Note that the linear-shaped lack-of-fusion pores can bring remarkable stress concentrations at the layer interfaces and thereby deteriorate the mechanical property of the as-built part [62,63].

For the good tracks with P = 150-200 W and $0.2 \text{ W}\cdot\text{min/mm} < P/\nu$ < 0.6 W min/mm (Fig. 2b), although near-full-density beads free of cracks or lack-of-fusion can be achieved, partial crystallization was observed. Specifically, for the samples with P = 150 W, v = 400 mm/min(i.e., $P/v = 0.375 \text{ W} \cdot \text{min/mm}$), and P = 175 W, v = 700 mm/min (i.e., P/v = 175 W), where V = 175 W is V = 175 W. $\nu = 0.25$ W·min/mm), the majority of the melt pool is featureless (amorphous) but marginal crystallization was found along the melt pool boundary. For the samples with P = 150 W, v = 250 mm/min (i.e., P/v =0.6 W·min/mm) and P=200 W, $\nu=1000$ mm/min (i.e., $P/\nu=0.2$ W·min/mm), severe crystallization throughout the entire melt pool was detected. The microstructures of these single-tracks with different degrees of crystallization will be discussed in detail in Section 3.2. These findings suggest that an overall higher linear energy density input promotes enhanced crystallization of MGs during LAM. In general, the linear energy density input in the melt pool is quantitively correlated with the average cooling rate (*R*) during LAM. For example, an inversely

exponential relationship of $R=1349 imes \left(\frac{p}{\nu}\right)^{-0.87}$ was measured during

LAM of $Zr_{39.6}Ti_{33.9}Nb_{7.6}Cu_{6.4}Be_{12.5}$ MG [64]. As such, it is understandable that a higher P/ν induces a lower cooling rate, which causes an increased probability of crystallization, and vice versa. Note that when multiple tracks or layers of MGs are printed, the re-heating induced crystallization in the heat affected zone should also be considered [65,66] in addition to the crystallization event during solidification studied in this work.

3.2. Microstructure characterization

After identifying the processing window for good single-tracks with no cracking or lack-of-fusion defects, we further analyzed the microstructures and elemental distributions in these tracks with different degrees of crystallization. Fig. 3 shows the microstructural morphology and associated elemental distribution in the single-track with marginal crystallization (P = 150 W, v = 400 mm/min). SEM-EDS mapping in the melt pool interior marked by the shallow-green box in Fig. 3a is displayed in Fig. 3b. It is seen that a number of spherical particles with an average diameter of approximately 1 µm were distributed uniformly in the amorphous matrix of the melt pool center. EDS mapping results in the melt pool interior indicate that elements distributions were relatively homogeneous with no apparent elemental segregation. The whole region was rich in Zr and a small amount of Fe was found. This is likely due to the Marangoni flow induced intermixing between the melt pool and the partially melted steel substrate as well as the thermal gradient induced chemical redistribution [36,58]. The average composition of the melt pool interior, represented by Region A in Fig. 3b, is summarized in Table 4, showing that Fe accounted for 7.3 at.%. Note that in this composition table, Be was not taken into consideration due to the difficulty in detecting such light elements by SEM-EDS. Fig. 3c shows the microstructure and elemental mapping of the melt pool boundary

marked by the shallow-orange box in Fig. 3a. Compared with the melt pool interior, crystalline particles were more densely distributed along the melt pool boundary. While Zr was barely revealed in the substrate, the distributions of all other elements including Fe, Ni, Ti, and Cu were more diffusive across the melt pool-substrate interface, suggesting the strong elemental mixing on both sides of the interface, which is essential for achieving a robust metallurgical bonding. The average composition of the melt pool boundary, represented by Region B in Fig. 3c, was also analyzed and summarized in Table 4. Surprisingly, compared with Region A in the melt pool interior, the content of Zr at the melt pool boundary significantly decreased from 52.6 at.% to 35.3 at.%, while the content of Fe almost quadrupled from 7.3 at.% to 27.1 at.%. To provide a macroscopic vision of the chemical composition throughout the entire melt pool, we performed line scans of the constituent elements from the melt pool to the substrate (Fig. 4). Elements were distributed uniformly in the melt pool center and substrate, respectively. However, gradual transitions in the elemental distributions were observed across the melt pool boundary, indicating the intermixing between the Vitreloy1 and the steel substrate. These results coincide well with the elemental mapping shown in Fig. 3. Note that the Marangoni flow and thermal gradient can not only cause inhomogeneous chemical redistribution but also introduce impurities from the substrate that serve as heterogeneous nucleation sites for crystallization, which may impair the glass forming ability of the MG, especially at the melt pool boundary. Hence, the LAM processing window to minimize crystallization can be substantially narrowed down [17,58]. This finding is particularly noteworthy when one considers the application of laser processing of MG coatings onto a dissimilar substrate material.

The above results suggest that chemical composition and crystallization behavior of the MG at the melt pool boundary are drastically different from that in the melt pool interior. In order to further investigate the differences in the crystallization products, we examined the crystal morphologies and their compositions in different regions of the good single-track with marginal crystallization, as shown in Fig. 5. Spherical crystals of $\sim 1~\mu m$ in size (Fig. 5b) were spread within the melt pool, whereas more refined dendrite-like crystals (\sim 0.2 μm) were present at the melt pool boundary (Fig. 5c). The chemical compositions of both representative crystals and the corresponding matrix are listed in Table 4. Zr was a dominant element in all the analyzed crystals, accounting for approximately 50 at.%. There was a larger proportion of Cu (21.0 \pm 6.0 at.%) in the spherical crystals than that in the dendritic crystals (14.2 \pm 3.9 at.%). Compared with the spherical crystals in the melt pool interior, the dendritic crystals at the melt pool boundary are featured by a much higher content of Fe, but less Ti. In addition, Fe became a major element of matrix at the melt pool boundary, which is in line with the aforementioned intermixing between the melt pool and the steel substrate. Since the Fe-Cu element pair presents distinct immiscibility with a large positive heat of mixing [67], the intermixing with Fe content in the melt pool is likely to have negative effect on the glass forming ability and contribute to more crystallization at the melt pool boundary where cracks frequently initiated. Furthermore, the addition of Fe from the substrate changed the Ti content, which is reported to

Table 4 Chemical composition (at.%) in the melt pool interior and at the melt pool boundary of the good single-track with marginal crystallization (P = 150 W, v = 400 mm/min). Region A and Region B correspond to the rectangle regions in Fig. 3b and c, respectively. The spherical and dendritic crystals reside within Region A and Region B, respectively, as marked in Fig. 5b and c.

Element Vitreloy1 alloy [39]		Melt pool inter	rior		Melt pool boundary		
		Region A	Spherical crystal	Matrix	Region B	Dendritic crystal	Matrix
Zr	41.2	52.6	44.7 ± 3.5	51.9 ± 0.6	35.3	49.0 ± 3.4	30.8 ± 1.1
Ti	13.8	16.6	15.4 ± 1.7	16.6 ± 0.3	10.5	9.8 ± 1.1	10.5 ± 0.5
Cu	12.5	13.0	21.0 ± 6.0	12.6 ± 0.5	14.0	14.2 ± 3.9	10.7 ± 1.3
Ni	10.0	10.5	11.7 ± 1.1	9.6 ± 0.2	13.1	13.3 ± 1.3	12.8 ± 0.4
Fe	_	7.3	8.5 ± 0.9	9.4 ± 1.0	27.1	13.7 ± 1.3	35.2 ± 1.2
Be	22.5	_	_	_	_	_	_

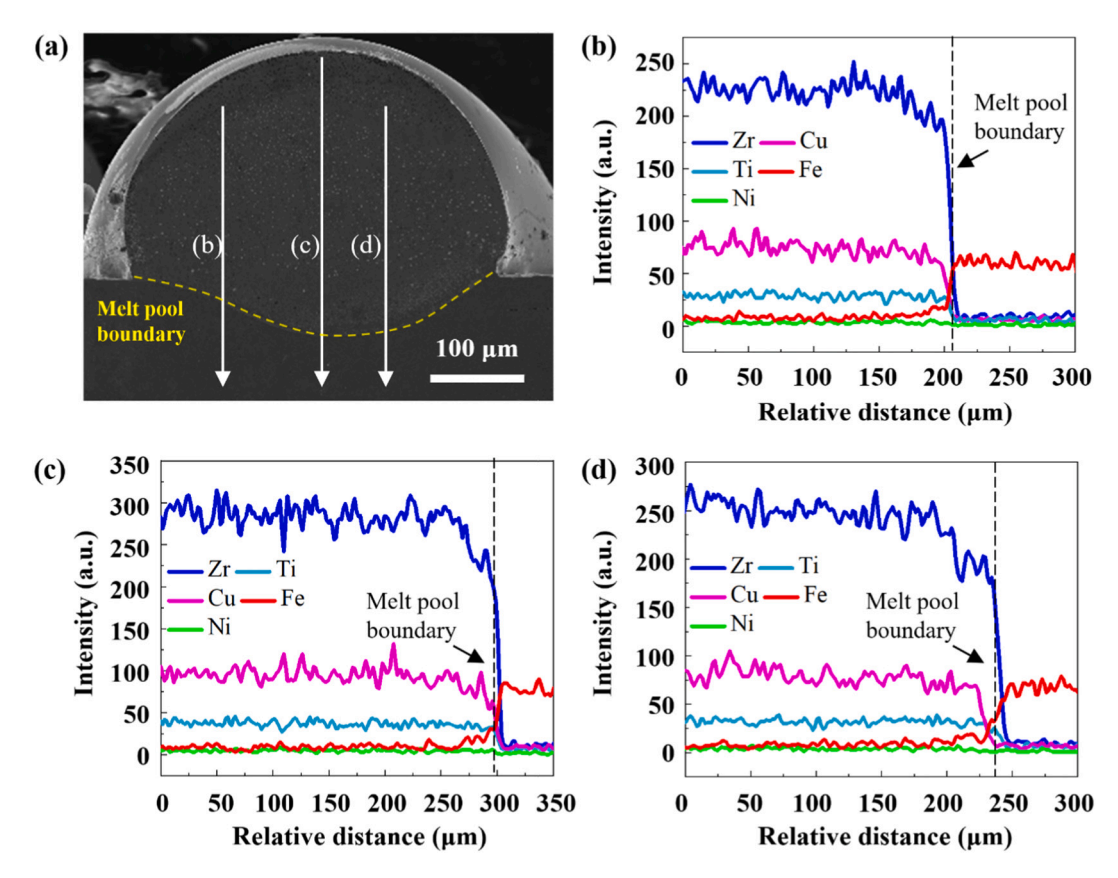


Fig. 4. (a) SEM micrograph of Vitreloy1 good single-track with marginal crystallization (P = 150 W, v = 400 mm/min). (b), (c), and (d) show the corresponding elemental distributions along the line scans marked in (a).

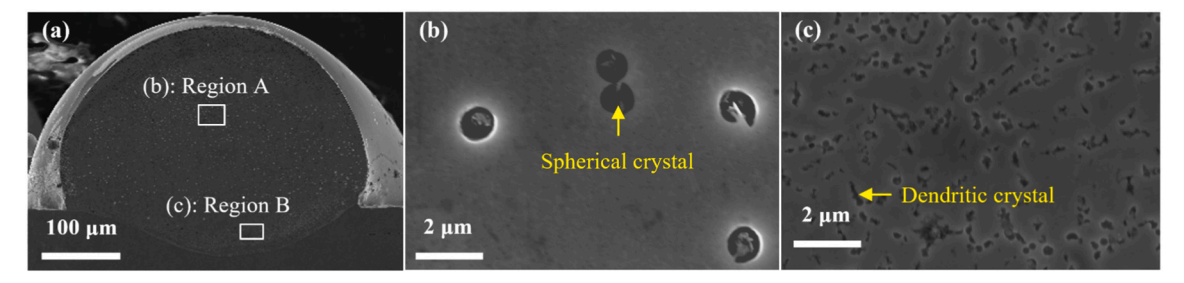


Fig. 5. (a) SEM micrograph of Vitreloy1 good single-track with marginal crystallization (P = 150 W, v = 400 mm/min). (b), and (c) are SEM micrographs showing enlarged areas in Region A and Region B. The chemical compositions of spherical crystal and dendritic crystal are listed in Table 4.

significantly affect GFA [68].

Fig. 6 displays the optical micrographs of Vitreloy1 good single-track with severe crystallization (P=150 W, $\nu=250$ mm/min). Massive crystals were revealed in this case. Specifically, the melt pool interior

mainly consisted of fine equiaxed dendritic crystals (Fig. 6a) while the melt pool boundary was comprised of a two-layered structure, planar layer with a thickness of $\sim 15 \,\mu\text{m}$ at the boundary and columnar dendrite layer inside the boundary (Fig. 6b). The width of the columnar dendrite

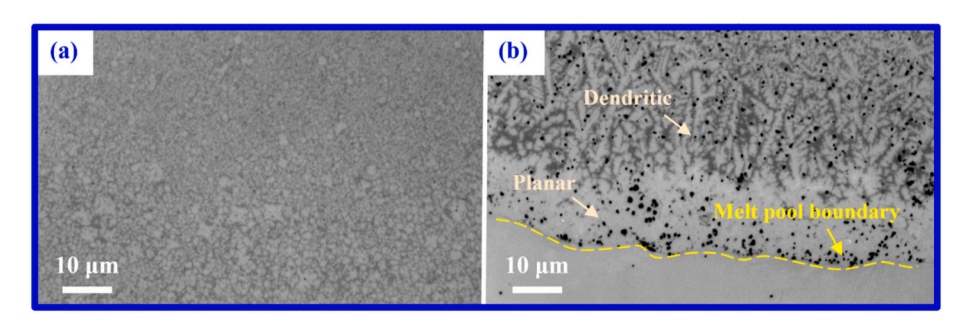


Fig. 6. Cross-sectional optical micrographs of good single-track with severe crystallization (P = 150 W, v = 250 mm/min) at (a) melt pool interior and (b) melt pool boundary.

near the melt pool boundary is about 1.9 μ m. Temperature gradient and solidification rate both have great impacts on the solidification microstructure during welding [56,69], so is the case in single-track printing. A combination of high temperature gradient and low solidification rate usually leads to planar structures while low temperature gradient and high solidification velocity promote equiaxed dendrites [56]. The solidification rate varies remarkably over the melt pool depth, from zero at the bottom of the melt pool boundary to the maximum (comparable to laser scanning speed) at the surface [57]. A typical transition in microstructural morphology from planar through columnar to equiaxed dendritic structures is a frequent signature in a rapidly solidified laser weld, in analogy to the microstructure of the severely crystallized single-track here [69].

3.3. Finite element simulation

The different solidification and crystallization behaviors and the evolution of processing defects are fundamentally related to the thermal history during LAM of MG. To gain an insight into the site-specific thermal history and cooling rate throughout the melt pool, numerical simulation was carried out for the good single-track sample with marginal crystallization (P = 150 W, v = 400 mm/min), which is used to elucidate the site-specific microstructures in the melt pool. As shown in Fig. 7a, the left part is the experiment result while the right part is the simulated peak temperature distribution from the substrate to the melt pool interior. The experimental and numerical single-track depths were similar, but the width of the simulated single-track was slightly larger than that in experiment. The width to depth ratio was 2.2 in experiment and 3.0 in simulation. Fig. 7b shows the thermal history for the positions of C1 ~ C6 in Fig. 7a. The peak temperature increased continuously from C1 to C6, and the cooling rates (bypassing the melting temperature of Vitreloy1 alloy, $T_l = 1001 \text{ K}$ [48]) are listed in Table 5. At the bottom position (C1), the cooling rate was found the smallest, 6726 K/s, and it increased with the distance away from the melt pool boundary. Higher cooling rates lead to greater volume fraction of amorphous solidification while lower cooling rates promote crystallization. The lower cooling

Table 5Cooling rates at different positions of the melt pool in the good single-track with marginal crystallization (Fig. 7a).

Position	Cooling rate (K/s)
C1	6726
C2	6803
C3	6979
C4	7033
C5	7121
C6	7242

rate near the melt pool boundary revealed by the thermal modeling is consistent with the fact that crystallization occurs preferentially from the melt pool boundary (Fig. 3).

In general, the linear energy density (P/ν) input can significantly affect the cooling rate and solidification microstructure, as we have observed that under the same power of 150 W, but different scanning speeds of 250 mm/min (i.e., $P/v = 0.6 \text{ W}\cdot\text{min/mm}$), 400 mm/min (i.e., $P/v = 0.375 \text{ W} \cdot \text{min/mm}$), and 1000 mm/min (i.e., $P/v = 0.15 \text{ W} \cdot \text{min/mm}$) mm) yield different features of severe crystallization, marginal crystallization, and lack-of-fusion. To understand the origin of this trend, we simulated the thermal histories for the three different P/v cases at the bottom of the melt pool boundary, as shown in Fig. 7c. The results turn out to be that the cooling rate was the slowest down to 3841 K/s in the sample with severe crystallization (150 W, 250 mm/min), and highest up to 12,148 K/s in the sample with lack-of-fusion (150 W, 1000 mm/ min), which agrees well with that there was severe crystallization occurring at sample of 150 W and 250 mm/min while there was negligible crystallized phase at sample of 150 W and 1000 mm/min. It is worth noting that the critical cooling rate to retain amorphous phase was reported to be of the order of 10 K/s or less [39], while the cooling rates in the melt pool of the simulated single tracks in this study were of more than the order of 10³ K/s. Besides the cooling rate, the higher linear energy density input may cause more Marangoni convection and hence chemical intermixing (Fig. 4). Such enhanced element diffusion

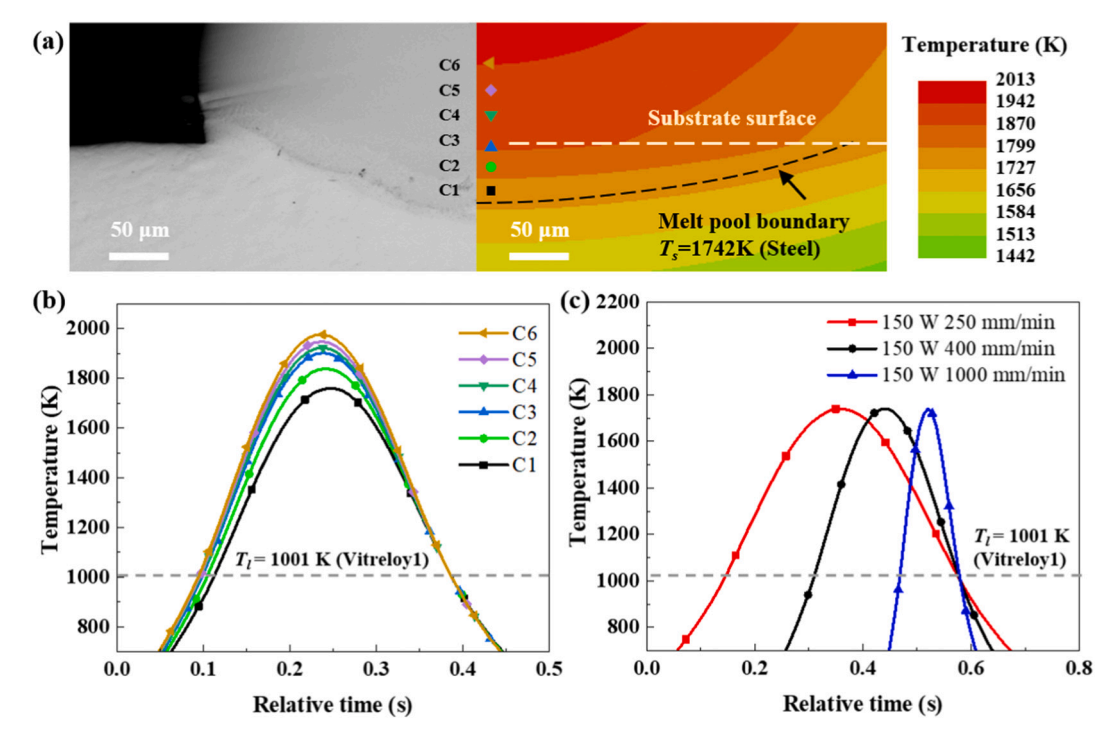


Fig. 7. (a) Cross section of the single-track with marginal crystallization (150 W, 400 mm/min) from numerical simulation with peak temperature contour and experiment results. (b) Transient temperature evolutions at different locations in (a). (c) Transient temperature evolutions at the bottom of the melt pool boundary in various samples: marginal crystallization (150 W, 400 mm/min), severe crystallization (150 W, 250 mm/min), and lack of fusion (150 W, 1000 mm/min).

could also elevate the crystallization. Therefore, at the vicinity of the melt pool boundary, the cooling rate and the chemical composition (intermixing) collectively influence the local crystallization behavior.

3.4. Microhardness

Microhardness measurements were carried out for the good singletracks from the substrate to the melt pool along the building direction (Fig. 8). Samples with marginal crystallization (P = 150 W, v = 400 mm/ min) and severe crystallization (P = 150 W, v = 250 mm/min) were both tested and then compared with fully amorphous Vitreloy1 alloy (560 HV) [70], marked by dash-dotted line. The optical micrograph in the inset illustrates the indentation locations. Overall, compared with the microhardness of 199 \pm 17 HV for the low carbon steel substrate, the MG melt pools showed significantly enhanced microhardness of approximately 700-1000 HV, suggesting that laser additively manufactured MG exhibits a high hardness that offers a great potential for coating applications. It is noted that microhardness of fully amorphous Vitreloy1 alloy was smaller than that in both cases, indicative of a positive effect of crystallization on the improvement of microhardness on Vitreloy1 alloy. Specifically, in the marginal crystallization sample, a drastic hardness peak of 1164 \pm 87 HV was observed at the melt pool boundary while in the severe crystallization sample the hardness throughout the entire melt pool (including the boundary) seemed to be more uniform. In the former sample, the melt pool was mainly amorphous, which exhibits a lower hardness of 705 \pm 48 HV in comparison with the locally crystallized melt pool boundary of 1164 \pm 87 HV. A significantly higher microhardness at the melt pool boundary than in the interior melt pool might be caused by element diffusion across the interface between the melt pool and the substrate, as indicated in Fig. 4. In addition, lower cooling rate at the melt pool boundary (Fig. 7b) tends to induce more crystallization, which may also contribute to higher microhardness. In the latter sample, the entire melt pool was severely crystallized, leading to the uniform hardness of approximately 930 HV. The difference in the average hardness of the melt pool for the two samples may arise due to the compositional and grain size differences in their crystallization products under different processing parameters. Higher scan speed (400 mm/min vs 250 mm/min) could create higher cooling rate, as indicated by Fig. 7c, and thus less crystallization would occur, leading to a lower average microhardness inside the melt pool (705 HV vs 930 HV). Note that the microhardness of the substrate below the melt pool boundary gradually reduced and stabilized to ~200 HV, which could be attributed to elemental intermixing between substrate and single-track or even microstructural/phase transformation (e.g., dynamic recrystallization) in the heat-affected zone [71].

4. Conclusions

We have conducted high-throughput laser single-track melting of Zr_{41 2}Ti_{13 8}Cu_{12 5}Ni_{10 0}Be_{22 5} metallic glass on low carbon steel with a wide range of laser powers and scanning speeds. A printability diagram was constructed to identify the optimal process window for achieving good single-tracks with minimal crystallization or processing defects such as cracking or lack-of-fusion. We found that cracking usually occurred at high powers (i.e., P > 200 W) or large linear energy densities (i.e., $P/v > 0.6 \text{ W} \cdot \text{min/mm}$) whereas lack-of-fusion tended to fall into the regions with lower powers (i.e., P < 150 W) or linear energy densities (i.e., $P/v < 0.2 \text{ W} \cdot \text{min/mm}$). Finite element thermal modeling was also performed to quantify the thermal history and cooling rate throughout the melt pool under different processing conditions in order to unravel the processing-microstructure relationship in the single-track library. The simulation results suggest that increasing linear energy density input during laser additive manufacturing can decrease the cooling rate and lead to more crystallization. For a given laser processing condition, the cooling rate inside the melt pool is highly site-specific. The melt pool boundary is featured by a lower cooling rate that leads

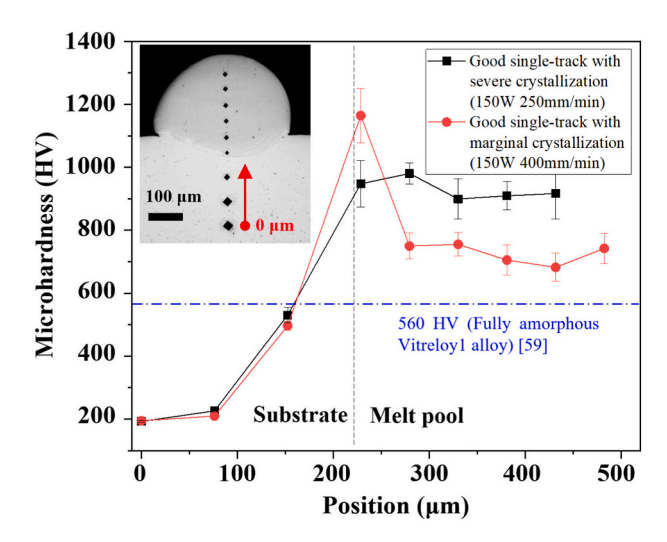


Fig. 8. Variation in the Vickers microhardness across the melt pool boundary along the building direction in the samples with marginal crystallization (150 W, 400 mm/min) and severe crystallization (150 W, 250 mm/min). 0 position represents the first point in the melt pool contiguous to the melt pool boundary. The inserted figure shows the optical micrograph of the distribution of indentation in the sample with the power of 150 W and the scanning speed of 400 mm/min. The dash-dotted line shows the Vickers microhardness of fully amorphous Vitreloy1 [70].

to enhanced partial crystallization, compared with the melt pool interior. In addition, we also performed microhardness tests and revealed significantly enhanced microhardness in the melt pool of MG in comparison with the substrate of low carbon steel, suggesting the promise of laser additive manufacturing of MG for wear-resistant coating applications. Our work provides significant insight into laser processing of MGs on a dissimilar crystalline substrate such as steel.

CRediT authorship contribution statement

Shengbiao Zhang: Investigation; Formal analysis; Writing - Original Draft.

Peijun Hou: Investigation; Formal analysis; Writing - Original Draft. **Shahryar Mooraj:** Investigation.

Wen Chen: Conceptualization; Visualization; Funding acquisition (financial support); Resources (Materials); Project administration; Supervision; Writing-Review & Editing.

Declaration of competing interest

The authors declare that they have no known competing financial interests or personal relationships that could have appeared to influence the work reported in this paper.

Acknowledgements

The authors acknowledge support from the National Science Foundation (CMMI-1927621 and DMR-2004429) and UMass Amherst Faculty Startup Fund. The authors are grateful to Prof. Jian Kong for providing the Vitreloy 1 powder samples.

References

- [1] S.F. Guo, J.L. Qiu, P. Yu, S.H. Xie, W. Chen, Fe-based bulk metallic glasses: brittle or ductile? Appl. Phys. Lett. 105 (2014), 161901 https://doi.org/10.1063/ 1.4899124.
- [2] C.A. Schuh, T.C. Hufnagel, U. Ramamurty, Mechanical behavior of amorphous alloys, Acta Mater. 55 (2007) 4067–4109, https://doi.org/10.1016/j. actamat.2007.01.052.

- [3] G. Kumar, H.X. Tang, J. Schroers, Nanomoulding with amorphous metals, Nature 457 (2009) 868–872, https://doi.org/10.1038/nature07718.
- [4] S.F. Guo, H.J. Zhang, Z. Liu, W. Chen, S.F. Xie, Corrosion resistances of amorphous and crystalline Zr-based alloys in simulated seawater, Electrochem. Commun. 24 (2012) 39–42, https://doi.org/10.1016/j.elecom.2012.08.006.
- [5] N. Li, W. Chen, L. Liu, Thermoplastic micro-forming of bulk metallic glasses: a review, JOM 68 (2016) 1246–1261, https://doi.org/10.1007/s11837-016-1844-y.
- [6] S. Mukherjee, J. Schroers, W.L. Johnson, W.-K. Rhim, Influence of kinetic and thermodynamic factors on the glass-forming ability of zirconium-based bulk amorphous alloys, Phys. Rev. Lett. 94 (2005), 245501, https://doi.org/10.1103/ PhysRevLett.94.245501.
- [7] Z.P. Lu, C.T. Liu, A new glass-forming ability criterion for bulk metallic glasses, Acta Mater. 50 (2002) 3501–3512, https://doi.org/10.1016/S1359-6454(02) 00166-0.
- [8] N. Li, J. Zhang, W. Xing, D. Ouyang, L. Liu, 3D printing of fe-based bulk metallic glass composites with combined high strength and fracture toughness, Mater. Des. 143 (2018) 285–296, https://doi.org/10.1016/j.matdes.2018.01.061.
- [9] T. DebRoy, H.L. Wei, J.S. Zuback, T. Mukherjee, J.W. Elmer, J.O. Milewski, A. M. Beese, A. Wilson-Heid, A. De, W. Zhang, Additive manufacturing of metallic components process, structure and properties, Prog. Mater. Sci. 92 (2018) 112–224, https://doi.org/10.1016/j.pmatsci.2017.10.001.
- [10] Z.-L. Chen, J.-M. Meng, Y. Cao, J.-L. Yin, R.-Q. Fang, S.-B. Fan, C. Liu, W.-F. Zeng, Y.-H. Ding, D. Tan, L. Wu, W.-J. Zhou, H. Chi, R.-X. Sun, M.-Q. Dong, S.-M. He, A high-speed search engine pLink 2 with systematic evaluation for proteome-scale identification of cross-linked peptides, Nat. Commun. 10 (2019) 3404, https://doi.org/10.1038/s41467-019-11337-z
- [11] Y.M. Wang, T. Voisin, J.T. McKeown, J. Ye, N.P. Calta, Z. Li, Z. Zeng, Y. Zhang, W. Chen, T.T. Roehling, R.T. Ott, M.K. Santala, P.J. Depond, M.J. Matthews, A. V. Hamza, T. Zhu, Additively manufactured hierarchical stainless steels with high strength and ductility, Nat. Mater. 17 (2018) 63–71, https://doi.org/10.1038/nmat5021
- [12] S. Peng, S. Mooraj, R. Feng, L. Liu, J. Ren, Y. Liu, F. Kong, Z. Xiao, C. Zhu, P. K. Liaw, W. Chen, Additive manufacturing of three-dimensional (3D)-architected CoCrFeNiMn high- entropy alloy with great energy absorption, Scr. Mater. 190 (2021) 46–51, https://doi.org/10.1016/j.scriptamat.2020.08.028.
- [13] Z. Mahbooba, L. Thorsson, M. Unosson, P. Skoglund, H. West, T. Horn, C. Rock, E. Vogli, O. Harrysson, Additive manufacturing of an iron-based bulk metallic glass larger than the critical casting thickness, Applied Materials Today. 11 (2018) 264–269, https://doi.org/10.1016/j.apmt.2018.02.011.
- [14] H. Chen, V.I. Levitas, L. Xiong, X. Zhang, Stationary dislocation motion at stresses significantly below the peierls stress: example of shuffle screw and 60- dislocations in silicon, Acta Mater. 206 (2021), 116623, https://doi.org/10.1016/j. actamat.2021.116623.
- [15] Z.W. Zhu, H.F. Zhang, H. Wang, B.Z. Ding, Z.Q. Hu, Influence of casting temperature on the thermal stability of cu- and zr-based metallic glasses: theoretical analysis and experiments, J. Mater. Res. 23 (2008) 2714–2719, https:// doi.org/10.1557/JMR.2008.0335.
- [16] S. Pauly, L. Löber, R. Petters, M. Stoica, S. Scudino, U. Kühn, J. Eckert, Processing metallic glasses by selective laser melting, Mater. Today 16 (2013) 37–41, https://doi.org/10.1016/j.mattod.2013.01.018.
- [17] X. Li, Additive manufacturing of advanced multi-component alloys: bulk metallic glasses and high entropy alloys, Adv. Eng. Mater. 20 (2018) 1700874, https://doi. org/10.1002/adem.201700874.
- [18] P. Bordeenithikasem, M. Stolpe, A. Elsen, D.C. Hofmann, Glass forming ability, flexural strength, and wear properties of additively manufactured Zr-based bulk metallic glasses produced through laser powder bed fusion, Addit. Manuf. 21 (2018) 312–317, https://doi.org/10.1016/j.addma.2018.03.023.
- [19] S. Pauly, C. Schricker, S. Scudino, L. Deng, U. Kühn, Processing a glass-forming Zr-based alloy by selective laser melting, Mater. Des. 135 (2017) 133–141, https://doi.org/10.1016/j.matdes.2017.08.070.
- [20] H. Sun, K.M. Flores, Laser deposition of a cu-based metallic glass powder on a zr-based glass substrate, J. Mater. Res. 23 (2008) 2692–2703, https://doi.org/10.1557/JMR.2008.0329.
- [21] H. Sun, K.M. Flores, Microstructural analysis of a laser-processed Zr-based bulk metallic glass, Metall. Mater. Trans. A 41 (2010) 1752–1757, https://doi.org/ 10.1007/s11661-009-0151-4.
- [22] Y. Li, Y. Shen, M.C. Leu, H.-L. Tsai, Building Zr-based metallic glass part on ti-6Al-4V substrate by laser-foil-printing additive manufacturing, Acta Mater. 144 (2018) 810–821, https://doi.org/10.1016/j.actamat.2017.11.046.
- [23] P. Bordeenithikasem, Y. Shen, H.-L. Tsai, D.C. Hofmann, Enhanced mechanical properties of additively manufactured bulk metallic glasses produced through laser foil printing from continuous sheetmetal feedstock, Addit. Manuf. 19 (2018) 95–103, https://doi.org/10.1016/j.addma.2017.11.010.
- [24] D. Ouyang, N. Li, W. Xing, J. Zhang, L. Liu, 3D printing of crack-free high strength zr-based bulk metallic glass composite by selective laser melting, Intermetallics 90 (2017) 128–134, https://doi.org/10.1016/j.intermet.2017.07.010.
- [25] P. Hou, Y. Li, W. Zhang, D. Chae, J.-S. Park, Y. Ren, Y. Gao, H. Choo, Synchrotron x-ray diffraction and crystal plasticity modeling study of martensitic transformation, texture development, and stress partitioning in deep-drawn TRIP steels, Materialia. 18 (2021), 101162, https://doi.org/10.1016/j.mtla.2021.101162.
- [26] J.J. Kruzic, Bulk metallic glasses as structural materials: a review, Adv. Eng. Mater. 18 (2016) 1308–1331, https://doi.org/10.1002/adem.201600066.
- [27] J. Ketkaew, Z. Liu, W. Chen, J. Schroers, Critical crystallization for embrittlement in metallic glasses, Phys. Rev. Lett. 115 (2015), 265502, https://doi.org/10.1103/ PhysRevLett.115.265502.

- [28] D. Wang, Y. Yang, X. Su, Y. Chen, Study on energy input and its influences on single-track, multi-track, and multi-layer in SLM, Int. J. Adv. Manuf. Technol. 58 (2012) 1189–1199, https://doi.org/10.1007/s00170-011-3443-y.
- [29] V. Matilainen, H. Piili, A. Salminen, T. Syvänen, O. Nyrhilä, Characterization of process efficiency improvement in laser additive manufacturing, Phys. Procedia 56 (2014) 317–326, https://doi.org/10.1016/j.phpro.2014.08.177.
- [30] W. Shi, Y. Liu, X. Shi, Y. Hou, P. Wang, G. Song, Beam diameter dependence of performance in thick-layer and high-power selective laser melting of ti-6Al-4V, Materials. 11 (2018) 1237, https://doi.org/10.3390/ma11071237.
- [31] Y. Li, K. Su, P. Bai, L. Wu, Microstructure and property characterization of Ti/ TiBCN reinforced ti based composite coatings fabricated by laser cladding with different scanning speed, Mater. Charact. 159 (2020), 110023, https://doi.org/ 10.1016/i.matchar.2019.110023.
- [32] P. Shurkin, T. Akopyan, A. Prosviryakov, A. Komissarov, N. Korotkova, Single track scanning experiment on the hypereutectic aluminium alloy Al-8%Zn-7%Ni-3%Mg, MATEC Web Conf. 326 (2020) 07001, https://doi.org/10.1051/matecconf/ 202032607001.
- [33] A. Aversa, M. Moshiri, E. Librera, M. Hadi, G. Marchese, D. Manfredi, M. Lorusso, F. Calignano, S. Biamino, M. Lombardi, M. Pavese, Single scan track analyses on aluminium based powders, J. Mater. Process. Technol. 255 (2018) 17–25, https://doi.org/10.1016/j.jmatprotec.2017.11.055.
- [34] J. Nie, C. Chen, L. Liu, X. Wang, R. Zhao, S. Shuai, J. Wang, Z. Ren, Effect of substrate cooling on the epitaxial growth of ni-based single-crystal superalloy fabricated by direct energy deposition, J. Mater. Sci. Technol. 62 (2021) 148–161, https://doi.org/10.1016/j.jmst.2020.05.041.
- [35] D.S. Gusev, A.B. Lyukhter, Influence of technological parameters on the geometry of single-track laser clad nickel based alloy on grey cast iron substrate, J. Phys. Conf. Ser. 941 (2017), 012037, https://doi.org/10.1088/1742-6596/941/1/ 012037
- [36] X.P. Li, C.W. Kang, H. Huang, L.C. Zhang, T.B. Sercombe, Selective laser melting of an Al86Ni6Y4.5Co2La1.5 metallic glass: processing, microstructure evolution and mechanical properties, Mater. Sci. Eng. A 606 (2014) 370–379, https://doi.org/ 10.1016/j.msea.2014.03.097.
- [37] N. Sohrabi, R.S. Panikar, J. Jhabvala, A.R. Buch, S. Mischler, R.E. Logé, Laser coating of a zr-based metallic glass on an aluminum substrate, Surf. Coat. Technol. 400 (2020), 126223. https://doi.org/10.1016/j.surfcoat.2020.126223.
- [38] X.P. Li, M. Roberts, Y.J. Liu, C.W. Kang, H. Huang, T.B. Sercombe, Effect of substrate temperature on the interface bond between support and substrate during selective laser melting of Al-Ni-Y-Co-La metallic glass, Materials & Design (1980-2015) 65 (2015) 1–6, https://doi.org/10.1016/j.matdes.2014.08.065.
- [39] A. Peker, W.L. Johnson, A highly processable metallic glass: Zr41.2Ti13.8Cu12.5Ni10.0Be22.5, Appl. Phys. Lett. 63 (1993) 2342–2344, https://doi.org/10.1063/1.110520.
- [40] Y. Han, L. Wang, K. Liu, W. Yan, Numerical modeling of laser powder bed fusion of metallic glasses: prediction of crystallization, J. Micromech. Mol. Phys. 05 (2020) 2050013, https://doi.org/10.1142/S2424913020500137.
- [41] I.A. Roberts, C.J. Wang, R. Esterlein, M. Stanford, D.J. Mynors, A three-dimensional finite element analysis of the temperature field during laser melting of metal powders in additive layer manufacturing, Int. J. Mach. Tools Manuf. 49 (2009) 916–923, https://doi.org/10.1016/j.ijmachtools.2009.07.004.
- [42] W. Huang, Y. Zhang, Finite element simulation of thermal behavior in single-track multiple-layers thin wall without-support during selective laser melting, J. Manuf. Process. 42 (2019) 139–148, https://doi.org/10.1016/j.jmapro.2019.04.019.
- [43] L. Liu, C. Zhang, Fe-based amorphous coatings: structures and properties, Thin Solid Films 561 (2014) 70–86, https://doi.org/10.1016/j.tsf.2013.08.029.
- [44] R. Wang, Z. Qin, F. Li, H., Xie, elastic behaviors of bulk metallic glass Zr41.2Ti13.8Cu12.5Ni10.0Be22.5 investigated by using ultrasonic technique, Chin. Phys. Lett. 14 (1997) 920, https://doi.org/10.1088/0256-307X/14/12/011.
- [45] A. Kalup, B. Smetana, M. Kawuloková, S. Zlá, H. Francová, P. Dostál, K. Waloszková, L. Waloszková, J. Dobrovská, Liquidus and solidus temperatures and latent heats of melting of steels, J. Therm. Anal. Calorim. 127 (2017) 123–128, https://doi.org/10.1007/s10973-016-5942-4.
- [46] T.L. Bergman, A.S. Lavine, D.P. DeWitt, Introduction to Heat Transfer, 6th Edition, Wiley, 2011.
- [47] R. Busch, Y.J. Kim, W.L. Johnson, Thermodynamics and kinetics of the undercooled liquid and the glass transition of the Zr41.2Ti13.8Cu12.5Ni10.0Be22.5 alloy, J. Appl. Phys. 77 (1995) 4039–4043, https://doi.org/10.1063/1.359485.
- [48] M. Yang, X.J. Liu, H.H. Ruan, Y. Wu, H. Wang, Z.P. Lu, High thermal stability and sluggish crystallization kinetics of high-entropy bulk metallic glasses, J. Appl. Phys. 119 (2016), 245112, https://doi.org/10.1063/1.4955060.
- [49] Y. Li, Y. Shen, C. Chen, M.C. Leu, H.-L. Tsai, Building metallic glass structures on crystalline metal substrates by laser-foil-printing additive manufacturing, J. Mater. Process. Technol. 248 (2017) 249–261, https://doi.org/10.1016/j. jmatprotec.2017.05.032.
- [50] W. Chen, T. Voisin, Y. Zhang, J.-B. Florien, C.M. Spadaccini, D.L. McDowell, T. Zhu, Y.M. Wang, Microscale residual stresses in additively manufactured stainless steel, Nat. Commun. 10 (2019) 4338, https://doi.org/10.1038/s41467-019-12265-8.
- [51] X.P. Li, C.W. Kang, H. Huang, T.B. Sercombe, The role of a low-energy-density rescan in fabricating crack-free Al85Ni5Y6Co2Fe2 bulk metallic glass composites via selective laser melting, Mater. Des. 63 (2014) 407–411, https://doi.org/10.1016/j.matdec.2014.06.022
- [52] E. Williams, N. Lavery, Laser processing of bulk metallic glass: a review, J. Mater. Process. Technol. 247 (2017) 73–91, https://doi.org/10.1016/j. jmatprotec.2017.03.034.

- [53] P. Hou, Y. Li, D. Chae, Y. Ren, K. An, H. Choo, Lean duplex TRIP steel: role of ferrite in the texture development, plastic anisotropy, martensitic transformation kinetics, and stress partitioning, Materialia. 15 (2021), 100952, https://doi.org/10.1016/j. mtla 2020 100952
- [54] J. Ren, C. Mahajan, L. Liu, D. Follette, W. Chen, S. Mukherjee, Corrosion behavior of selectively laser melted CoCrFeMnNi high entropy alloy, Metals. 9 (2019) 1029, https://doi.org/10.3390/met9101029.
- [55] W. Chen, Z. Liu, J. Ketkaew, R.M.O. Mota, S.-H. Kim, M. Power, W. Samela, J. Schroers, Flaw tolerance of metallic glasses, Acta Mater. 107 (2016) 220–228, https://doi.org/10.1016/j.actamat.2016.02.002.
- [56] J.C. Lippold, Welding Metallurgy and Weldability, John Wiley & Sons, 2014.
- [57] M. Gremaud, M. Carrard, W. Kurz, The microstructure of rapidly solidified Al-Fe alloys subjected to laser surface treatment, Acta Metall. Mater. 38 (1990) 2587–2599, https://doi.org/10.1016/0956-7151(90)90271-H.
- [58] N. Sohrabi, R.S. Panikar, J. Jhabvala, A.R. Buch, S. Mischler, R.E. Logé, Laser coating of a Zr-based metallic glass on an aluminum substrate, Surf. Coat. Technol. 400 (2020), 126223, https://doi.org/10.1016/j.surfcoat.2020.126223.
- [59] W. Chen, Z. Liu, H.M. Robinson, J. Schroers, Flaw tolerance vs. Performance: a tradeoff in metallic glass cellular structures, Acta Mater. 73 (2014) 259–274, https://doi.org/10.1016/j.actamat.2014.04.026.
- [60] L. Johnson, M. Mahmoudi, B. Zhang, R. Seede, X. Huang, J.T. Maier, H.J. Maier, I. Karaman, A. Elwany, R. Arróyave, Assessing printability maps in additive manufacturing of metal alloys, Acta Mater. 176 (2019) 199–210, https://doi.org/ 10.1016/j.actamat.2019.07.005.
- [61] M. Letenneur, A. Kreitcberg, V. Brailovski, Optimization of laser powder bed fusion processing using a combination of melt Pool modeling and Design of Experiment Approaches: density control, J. Manuf. Mater. Process. 3 (2019) 21, https://doi. org/10.3390/immp3010021.
- [62] M. Neikter, F. Forsberg, R. Pederson, M.-L. Antti, P. Åkerfeldt, S. Larsson, P. Jonsén, G. Puyoo, Defect characterization of electron beam melted ti-6Al-4V and

- alloy 718 with X-ray microtomography, Aeronaut. Aerosp. Open Access J. 2 (2018) 139–145
- [63] T. Montalbano, B.N. Briggs, J.L. Waterman, S. Nimer, C. Peitsch, J. Sopcisak, D. Trigg, S. Storck, Uncovering the coupled impact of defect morphology and microstructure on the tensile behavior of ti-6Al-4V fabricated via laser powder bed fusion, J. Mater. Process. Technol. 294 (2021), 117113, https://doi.org/10.1016/j. imatprotec.2021.117113.
- [64] Y. Lu, S. Su, S. Zhang, Y. Huang, Z. Qin, X. Lu, W. Chen, Controllable additive manufacturing of gradient bulk metallic glass composite with high strength and tensile ductility, Acta Mater. 206 (2021), 116632, https://doi.org/10.1016/j. actamat.2021.116632.
- [65] C. Zhang, D. Ouyang, S. Pauly, L. Liu, 3D printing of bulk metallic glasses, Materials Science and Engineering: R: Reports. 145 (2021), 100625, https://doi. org/10.1016/j.mser.2021.100625.
- [66] D. Ouyang, P. Zhang, C. Zhang, L. Liu, Understanding of crystallization behaviors in laser 3D printing of bulk metallic glasses, Appl. Mater. Today 23 (2021), 100988, https://doi.org/10.1016/j.apmt.2021.100988.
- [67] Q.S. Zhang, W. Zhang, A. Inoue, Ni-free Zr–Fe–Al–Cu bulk metallic glasses with high glass-forming ability, Scr. Mater. 61 (2009) 241–244, https://doi.org/ 10.1016/j.scriptamat.2009.03.056.
- [68] P. Tsai, K.M. Flores, High-throughput discovery and characterization of multicomponent bulk metallic glass alloys, Acta Mater. 120 (2016) 426–434, https://doi.org/10.1016/j.actamat.2016.08.068.
- [69] D.A. Porter, K.E. Easterling, Phase Transformations in Metals and Alloys, CRC Press, 2009
- [70] K. Lee, E. Yun, S. Lee, N.J. Kim, et al., Two-layered Zr-Base amorphous Alloy/Metal surface composites fabricated by high-energy electron-beam irradiation, Metall. Mater. Trans. A Phys. Metall. Mater. Sci. 35A (2004) 3455–3460.
- [71] I. Miraoui, M. Boujelbene, M. Zaied, High-power laser cutting of steel plates: heat affected zone analysis, Adv. Mater. Sci. Eng. 2016 (2016), e1242565, https://doi. org/10.1155/2016/1242565.